

# Two-dimensional Kondo lattice in a TaS<sub>2</sub> van der Waals heterostructure

Cosme G. Ayani<sup>1,2</sup>, Michele Pisarra<sup>3</sup>, Iván M. Ibarburu<sup>1</sup>, Manuela Garnica<sup>2,6</sup>, Rodolfo Miranda<sup>1,2,4,6</sup>, Fabián Calleja<sup>2,\*</sup>, Fernando Martín<sup>2,4,5</sup>, Amadeo L. Vázquez de Parga<sup>1,2,4,6,\*</sup>

## Affiliations:

<sup>1</sup>Departamento de Física de la Materia Condensada, Universidad Autónoma de Madrid, Cantoblanco 28049, Madrid, Spain.

<sup>2</sup>IMDEA Nanociencia, Calle Faraday 9, Cantoblanco 28049, Madrid, Spain.

<sup>3</sup>INFN, Sezione LNF, Gruppo collegato di Cosenza, Cubo 31C, 87036 Rende (CS), Italy.

<sup>4</sup>IFIMAC, Universidad Autónoma de Madrid, Cantoblanco 28049, Madrid, Spain

<sup>5</sup> Dep. Química Módulo 13, Universidad Autónoma de Madrid, Cantoblanco, 28049 Madrid, Spain.

<sup>6</sup> Instituto Nicolás Cabrera, Universidad Autónoma de Madrid, Cantoblanco, 28049, Madrid, Spain

**Strongly correlated materials exhibit exotic electronic states arising from the strong correlation between electrons. Dimensionality provides a tuning knob because thinning down to atomic thickness reduces screening effects and enhances electron correlations. In this work, a 2D Kondo lattice has been created by stacking a layer of 1T-TaS<sub>2</sub> on a 2H-TaS<sub>2</sub> crystal, which are bound by weak van der Waals interactions. By using high-resolution scanning tunnelling spectroscopy and density functional theory, we unambiguously demonstrate the formation of a 2D Kondo lattice from an ensemble of independent Kondo impurities present at higher temperatures. The possibility to create 2D Kondo lattices in van der Waals heterostructures paves the way for the exploration of unconventional metallic, magnetic and superconducting states not present in more standard correlated materials.**

Solids containing strongly correlated electrons present a rich variety of ground state properties resulting from complex many-body interactions. The interplay between charge, spin and orbital degrees of freedom gives rise to unusual phenomena, as the coexistence of superconductivity and magnetism [1,2], the appearance of multiple superconducting phases with different order parameters [3,4] and the existence of mixed valence states [5]. The manipulation of electron correlations in these materials has direct implications in the development of superconducting magnets, magnetic storage, Mott transistors and sensing [6,7].

Among the existing strongly correlated materials, the heavy fermion compounds containing 4f and 5f electrons are the ones with the strongest electron correlation in the ground state [8], where the

interplay between the f-shell and conduction electrons gives rise to two competing effects: the Ruderman-Kittel-Kasuya-Yosida (RKKY) interaction [9-11], which favors long-range magnetic order, and the Kondo effect [12-14], which leads to demagnetization. The former is the consequence of the indirect exchange coupling between localized spins and the latter of the on-site screening produced by the conduction electrons. In principle, the resulting ground state can be either magnetically ordered or a paramagnetic Kondo lattice, depending on the relative strength of the Kondo coupling and the RKKY interaction, as described by the Doniach phase diagram [15]. Most heavy-fermion crystals form a three-dimensional lattice that allows for antiferromagnetic ordering [16-20]. However, specific geometry constraints or the reduction of the dimensionality, as in 2D materials, surfaces and/or interfaces, might forbid the formation of ordered arrangements, giving rise to frustrated spin lattices. The importance of magnetic frustration in heavy fermion physics has been discussed theoretically [21]. However, crystals of f-electron metals with geometrically frustrated lattices is very limited [17]. We demonstrate the engineering of a 2D geometrically frustrated Kondo lattice using an atomically thin layer of a transition metal dichalcogenide with spins spatially localized by a CDW interacting with a sea of conduction electrons from the underlying metallic transition dichalcogenide.

In short, the physics of the two competing mechanisms mentioned above can be described as follows. When a spin-half electronic state of an isolated magnetic impurity is embedded in the conduction bands of a metal, the interaction with the conduction electrons leads to the formation of a singlet spin state as shown in Fig. 1a [12-14]. The “Kondo singlet” formation is revealed in the Local Density Of States (LDOS) as an intense zero-bias feature, the Kondo resonance, sketched as a sharp peak in Fig. 1b. The intensity of the Kondo resonance rapidly increases upon cooling to temperatures below the characteristic Kondo temperature ( $T_K$ ). Figure 1b shows schematically the singly occupied electronic state of the impurity,  $\epsilon_d$ , and the energy needed to bring an additional electron from an occupied state of the metal at the Fermi energy  $E_F$  into the impurity electronic state,  $\epsilon_d+U$

A Kondo lattice is an ordered dense arrangement of magnetic moments coupled with the conduction electrons. Theoretical predictions of the possible existence of Kondo lattices and the physics behind this phenomenon date from as early as the 1980s [22,23]. In Kondo lattices, for temperatures well below  $T_K$ , the Kondo clouds of the individual impurities become coherently superimposed and acquire the periodicity of the crystal. This is the consequence of the

hybridization of the conduction electrons with the localized magnetic impurities, which results in the loss of the magnetic moments, as sketched in Fig. 1c. The electrons, originally localized at the magnetic impurities, are thus delocalized and form part of the new Fermi surface, while at the same time the conduction electrons of the crystal acquire very large effective masses. The energy scale for the Kondo lattice formation is given by a characteristic temperature  $T_{KL}$ , expected to be lower than  $T_K$ , because once lost the magnetic moments, the magnetic interaction between impurities is no longer in operation. Hence, the energy gain per site due to the Kondo lattice development is smaller than the energy gain for a single Kondo resonance [24]. The corresponding LDOS at the Fermi level is expected to exhibit a more complex gap-like structure [22], as depicted in Fig. 1d in contrast with the single peak related to the single Kondo impurity regime (Fig. 1b).

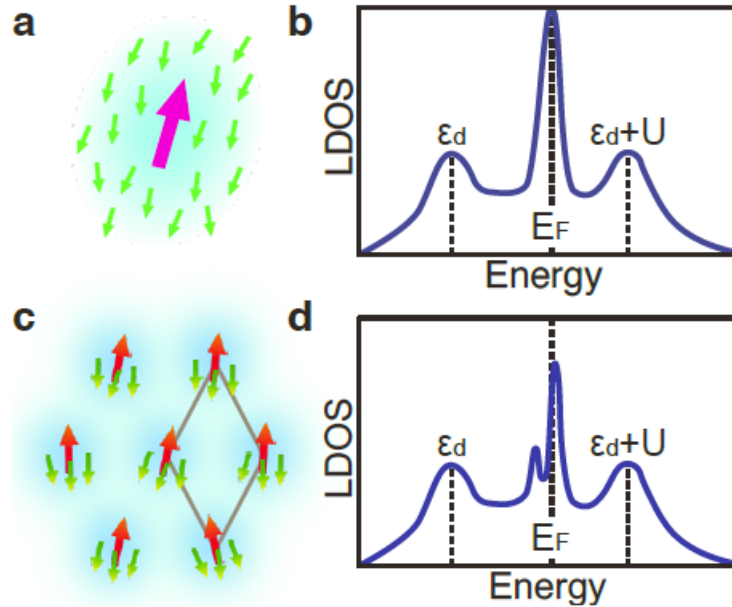


**Figure 1: Single Kondo impurity and Kondo lattice.** **a** Schematic representation of a single-impurity Kondo effect. The red arrow represents the spin of the impurity and the green arrows the spins of the conduction electrons. **b** LDOS corresponding to a. **c** Schematic representation of a Kondo lattice formed from an array of impurities. Same conventions as in a. **d** LDOS corresponding to c. In panels b and d  $\epsilon_d$  shows the energy position of the impurity single occupied electronic state, while  $\epsilon_d + U$  represents the energy needed for the double occupancy of that state.

The invention of the scanning tunnelling microscope (STM) has allowed for the experimental exploration of the Kondo physics on individual magnetic adatoms or charged organic molecules [25-27]. In this work, we show, by means of STM and its related spectroscopy (STS), clear evidence of the formation of a 2D Kondo lattice by stacking a 1T-TaS<sub>2</sub> layer on a 2H-TaS<sub>2</sub> crystal. We image the ordered array of Kondo resonances at around 1.5 K, well below the Kondo

temperature and we follow the evolution in the LDOS from the Kondo lattice regime to the single Kondo impurity regime as we ramp up the temperature across  $T_{KL}$ . The observed modifications in the LDOS are well explained by state-of-the-art DFT calculations.

TaS<sub>2</sub> is a transition metal dichalcogenide with a quasi-two-dimensional character [28, 29], which has two basic structures: a 2H-TaS<sub>2</sub> structure where the coordination between the Ta and S atoms is trigonal prismatic, and a 1T-TaS<sub>2</sub> structure with an octahedral coordination [28]. These polymorphs are very close in formation energy [30]. 2H-TaS<sub>2</sub> undergoes an in-plane transition around 78 K with a long-range order quasi-commensurate (3×3) charge density wave (CDW) [31] established on the sample's surface, causing the opening of a pseudo gap at the Fermi level due to the incomplete nesting in the 2D Fermi surface [32,33]. 1T-TaS<sub>2</sub> presents, below 180 K, a commensurate CDW with a periodicity of  $(\sqrt{13} \times \sqrt{13})R13,9^\circ$  [29]. The atomic structure consists in clusters of 13 Ta atoms in which the 12 outer atoms are slightly displaced towards the central one, forming a Star-of-David (SoD) cluster [29]. The 5d orbitals from the 12 outer Ta atoms form the valence and conduction bands separated by the CDW gap [34, 35]. The remaining orbital, corresponding to the Ta atom at the center of the SoD, forms a half-filled band, suggesting a metallic character of the 1T-TaS<sub>2</sub> structure in the ground state [36]. However, experimentally, this structure is found to be insulating [34, 37], which has been attributed to a Mott localization of the remaining single electron at the center of the SoD [38]. The Mott localization splits the band at the Fermi level in two Hubbard sub-bands separated by a Mott-Hubbard gap [36].

## Results

A 2H-TaS<sub>2</sub> single crystal was cleaved and inserted in the low temperature STM without breaking the Ultra-High Vacuum (UHV) conditions (see Experimental Methods). The sample presents terraces of the order of 2 μm wide separated by single layer steps, as can be seen in the large scale STM images (see Supplementary Information (SI) section 1). Most of the surface presents a quasi-commensurate (3×3) CDW as expected for a 2H-TaS<sub>2</sub> single crystal [31]. Due to the close values of the formation energy for the 2H-TaS<sub>2</sub> and the 1T-TaS<sub>2</sub> polymorphs [30], it was possible to find, in the 2H-TaS<sub>2</sub> crystal, areas where the topmost layer exhibits a 1T-TaS<sub>2</sub> structure. Figure 2a shows a representative STM image with a single layer step-edge separating two atomic terraces. The lower terrace (right-hand side) presents the quasi-(3×3) CDW periodicity expected for a 2H-TaS<sub>2</sub> crystal. An atomically resolved STM image measured on this terrace can be seen in the inset on the right. Both the atomic (green rhombus) and the CDW (blue rhombus) periodicities are

indicated. The upper (left-hand side) terrace presents a different long-range periodicity, namely  $(\sqrt{13} \times \sqrt{13})R13,9^\circ$ , which corresponds to the CDW present at low temperature on 1T-TaS<sub>2</sub>. The left inset in Fig. 2a shows an atomically resolved image measured on the upper terrace. The structure of the SoD unit cell is superimposed to the topographic image on its lower right corner. Figure 2b shows a line profile measured across the step, with an apparent step height of  $619 \pm 50$  pm, corresponding to a single layer of TaS<sub>2</sub>. The corrugation associated with the  $(\sqrt{13} \times \sqrt{13})R13,9^\circ$  periodic structure can be seen in the profile, while that of the quasi-(3×3) periodicity is not visible due to its intrinsic low magnitude in the STM images. The discrimination of the other possible 1T/1T scenarios and the determination of the periodicity of both CDWs by STM is described in detail in sections 2 and 3 of the SI, respectively.

The right panel in Fig. 2c shows the STS spectroscopy data measured at 1.2 K on a terrace presenting the quasi-(3×3) CDW, with a sketch illustrating the stacking sequence on those terraces. The expected width of the pseudo gap associated to the CDW [32] is marked with dashed vertical lines. The left panel in Fig. 2c shows the STS spectra measured on the terrace presenting the  $(\sqrt{13} \times \sqrt{13})R13,9^\circ$  CDW, and the corresponding sketch of the stacking sequence. The Upper and Lower Hubbard sub-bands (marked as UHB and LHB) can be seen on both sides of the Fermi level. A third spectral feature is a sharp peak that appears close to the Fermi level. The STS spectra measured at 52 K on these 1T/2H areas still show the Hubbard sub-bands but the peak at the Fermi level is no longer present (see SI section 4). We identify this peak as a Kondo resonance, resulting from the screening of the localized electrons at the center of the SoD clusters by the conduction electrons from the metallic substrate [39, 40].

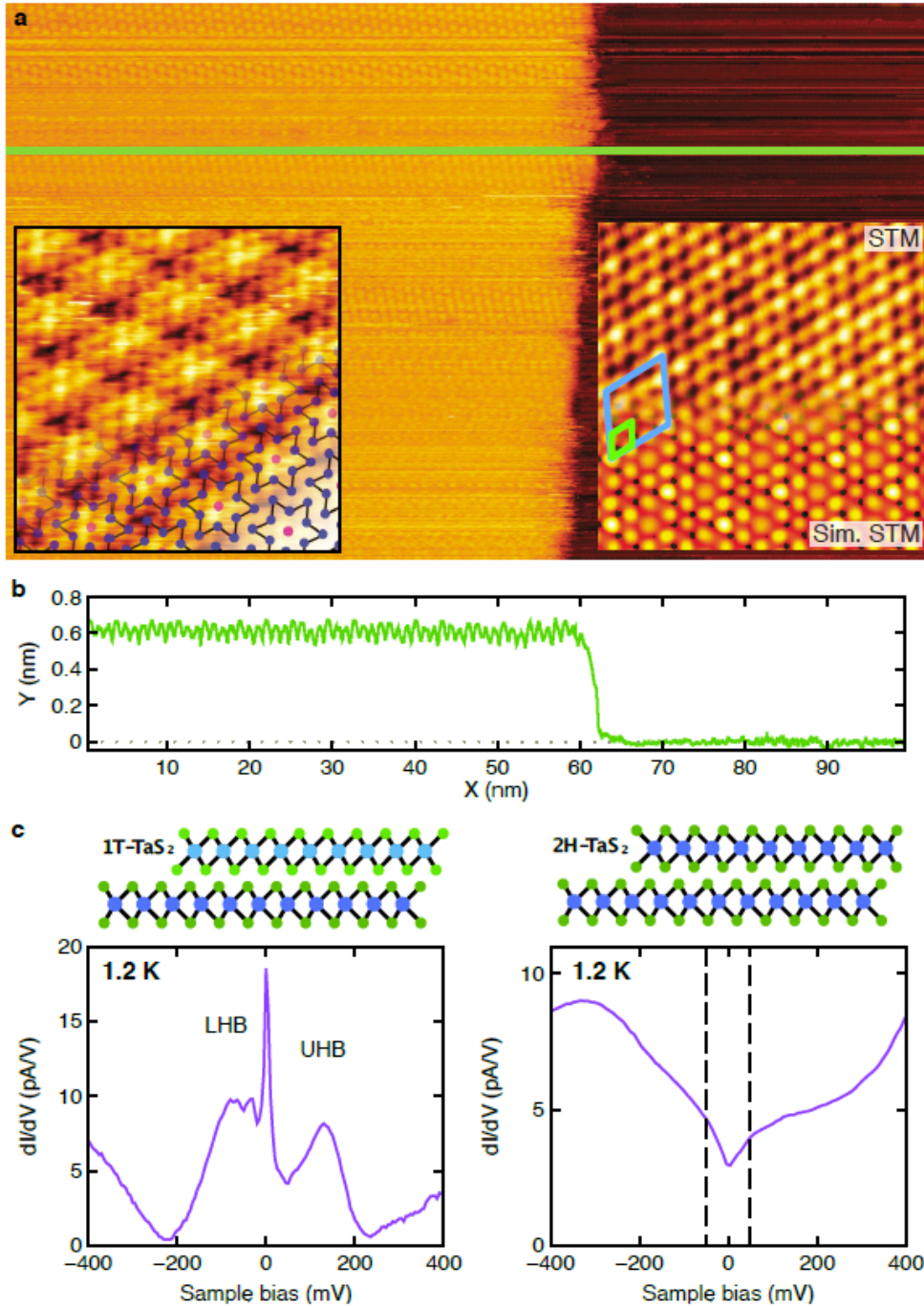


**Figure 2: 1T/2H Heterostructure.** **a** Large scale STM topographic image showing two terraces on the 2H-TaS<sub>2</sub> surface separated by a single layer step-edge. Image parameters:  $V_b = 500$  mV,  $I_t = 300$  pA, size 100 nm x 60 nm. The terraces present different surface periodicities. The inset on the left-hand side shows an atomically resolved STM image acquired on the corresponding upper terrace. The  $\sqrt{13} \times \sqrt{13} R13.9^\circ$  CDW periodicity is clearly seen on the image, where a model of the SoD structure is superimposed. Image parameters:  $V_b = 500$  mV,  $I_t = 300$  pA, size 18 nm x 18 nm. The inset on the right-hand side shows the quasi-(3×3) CDW present on the lower terrace and the simulated STM image resulting from the DFT calculations (see section 11 in the SI). The atomic periodicity is marked with the green rhombus and the quasi-(3×3) CDW with the blue rhombus. Image parameters:  $V_b = -50$  mV,  $I_t = 200$  pA, size 15 nm x 15 nm. **b** Line profile across

the step edge shown in panel a with a solid green line, the single layer step-edge has a height of  $619 \pm 50$  pm. **c** Left-hand side: Model of the stacking sequence on the upper terrace showing a 1T-TaS<sub>2</sub> single layer on top of a 2H-TaS<sub>2</sub> crystal. The lower panel shows the STS performed on a 1T-TaS<sub>2</sub> area of the sample at 1.2 K. STS parameters:  $V_b = 400$  mV,  $I_t = 500$  pA,  $V_{mod}=4$  mV. The upper and lower Hubbard sub-bands are marked (UHB and LHB respectively), a sharp resonance appears close to the Fermi level. On the right-hand side the upper panel shows a scheme of the local stacking 2H polytype area of TaS<sub>2</sub>. The lower panel shows the corresponding STS spectrum measured at 1.2 K, the pseudo gap produced by the quasi-(3×3) CDW is observed around zero bias (dashed vertical lines). STS parameters:  $V_b = 400$  mV,  $I_t = 500$  pA,  $V_{mod}=10$  mV.

Figure 3 shows the periodic spatial modulation in the intensity of the Kondo peak within the unit cell of the  $(\sqrt{13} \times \sqrt{13})R13.9^\circ$  CDW. The inset shows the corresponding STM topography, with colored dots indicating the location where the representative STS spectra were measured. The Kondo resonance is more pronounced when the tip is located at the center of the SoD and its intensity drops rapidly when the tip moves slightly off center. The temperature evolution of the Kondo resonance, analyzed in sections 6 and 7 of the SI, gives a Kondo temperature of 28 K, in agreement with the fact that no Kondo resonance is detected at 52K (SI section 4).

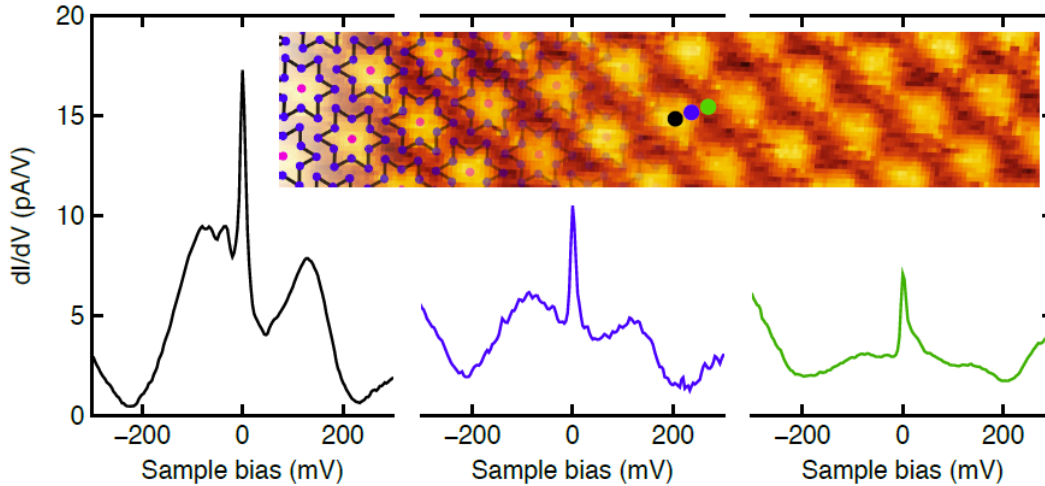


**Figure 3: Spatial modulation of the Kondo resonance.** Single point STS taken at 1.5K on different locations along the CDW unit cell, showing the modulation of the intensity of the zero bias Kondo peak. The Kondo resonance is more intense at the centre of the SoD (black spectrum) and its intensity drops away from the center (blue and green spectra). STS parameters:  $V_b = 500$  mV,  $I_t = 500$  pA,  $V_{mod} = 4$  mV. The inset shows the area of the sample where the spectra were measured. Image parameters:  $V_b = 500$  mV,  $I_t = 90$  pA, size 20 nm × 4 nm.

When the 1T-TaS<sub>2</sub> single layer is placed on top of the 2H-TaS<sub>2</sub> substrate the system has all the key ingredients to develop a Kondo lattice. For temperatures below  $T_K = 28$  K, the unpaired electrons localized at the center of the SoD clusters are Kondo screened by the metallic 2H-TaS<sub>2</sub> substrate. At the same time, the  $(\sqrt{13} \times \sqrt{13})R13.9^\circ$  CDW imposes a triangular 2D lattice with spatial long-range order [41] that frustrates a possible antiferromagnetic arrangement of the magnetic moments

located at the center of the SoD. As discussed before, the formation of the Kondo lattice modifies the Fermi surface of the system in order to include in the periodic system the localized electrons. In Fig. 4a we present a high-resolution STS spectrum measured on the heterostructure at 1.5 K using a bias modulation of 200  $\mu\text{V}$ , which shows the appearance of a double peak structure related to the Kondo lattice gap (see Fig. 1d). Note that this feature is barely visible in the spectra measured with a larger (4 mV) bias modulation (see Fig. 2 and section 7 in the SI).

The formation of a Kondo lattice with the corresponding appearance of the heavy-fermion liquid phase can be considered as the result of the hybridization of the flat band originating from the unpaired electrons localized at the magnetic impurities and the dispersing bands describing the conduction electrons of the metallic substrate. The main physics of the system can be described by the effective Hamiltonian [22]:

$$H = \sum_{kn} \epsilon_{kn} d_{kn}^\dagger d_{kn} + \sum_k \epsilon_{ki} c_{ki}^\dagger c_{ki} + \sum_{kn} (\langle i | \hat{V}_k | n \rangle c_{kni}^\dagger d_{kn} + h.c.) \quad (1)$$

where  $\mathbf{k}$  is a reciprocal lattice vector inside the first Brillouin Zone,  $d_{kn}^\dagger$  and  $d_{kn}$  are fermionic operators for the conduction band  $\epsilon_{kn}$  (with  $n$  a multi-index including multiple bands and spin) of the substrate;  $c_{ki}^\dagger$  and  $c_{ki}$  are the fermionic operators of the lattice of impurity states, with energies  $\epsilon_{ki}$ , after they establish coherence (the ‘‘impurity band’’); and  $\hat{V}_k$  is the interaction potential, which, in general, depends on  $\mathbf{k}$  and might be different for different conduction bands (see also SI section 11).

The 2H-TaS<sub>2</sub> crystals are metallic due to two doubly degenerate bands crossing the Fermi level that originate from the Ta 5d half-filled orbitals. The dispersion of these bands is slightly modified by the formation of a quasi-(3 $\times$ 3) CDW [29, 33]. A detailed analysis of the electronic properties of bulk 2H-TaS<sub>2</sub> based on Density Functional Theory (DFT) calculations is provided in Theoretical Methods and sections 12 and 15 of the SI. As can be seen in the right inset of Fig. 2a, these calculations reproduce fairly well the CDW of 2H-TaS<sub>2</sub>. The corresponding bands have been used as conduction bands  $\epsilon_{kn}$  in (1). The impurity band  $\epsilon_{ki}$ , on the other hand, appears with the  $(\sqrt{13} \times \sqrt{13})R13.9^\circ$  periodicity of the SoD CDW in the 1T-TaS<sub>2</sub> overlayer, and is ‘‘made of’’ electrons from the 2H-TaS<sub>2</sub> substrate, which screen the magnetic impurities of the 1T overlayer. Since very little is known a priori about this band, we have assumed a band dispersion typical of TaS<sub>2</sub> with a  $\sim 40$  meV total band width and a periodicity commensurate to the (3 $\times$ 3) 2H-TaS<sub>2</sub> lattice, which is justified by the narrow width of this band and allows keeping the computational

cost at a manageable level. In Fig. 4 we provide the band structure (panels b and c) and the DOS (panel d), as obtained by numerically diagonalizing the Hamiltonian in equation (1) with a ( $k$ -independent)  $V = |\hat{V}_k| = 5$  meV interaction potential between the impurity band and *all* the conduction bands of the  $(3 \times 3)$  2H-TaS<sub>2</sub> surface. In Fig. 4c, the opening of gaps around the Fermi level resulting from the avoided band-crossing can be seen. Figure 4d shows the resulting LDOS. A double peak structure is found near the Fermi level as opposed to the single peak structure obtained when the interaction potential was switched-off (see Fig.S15 of the SI).

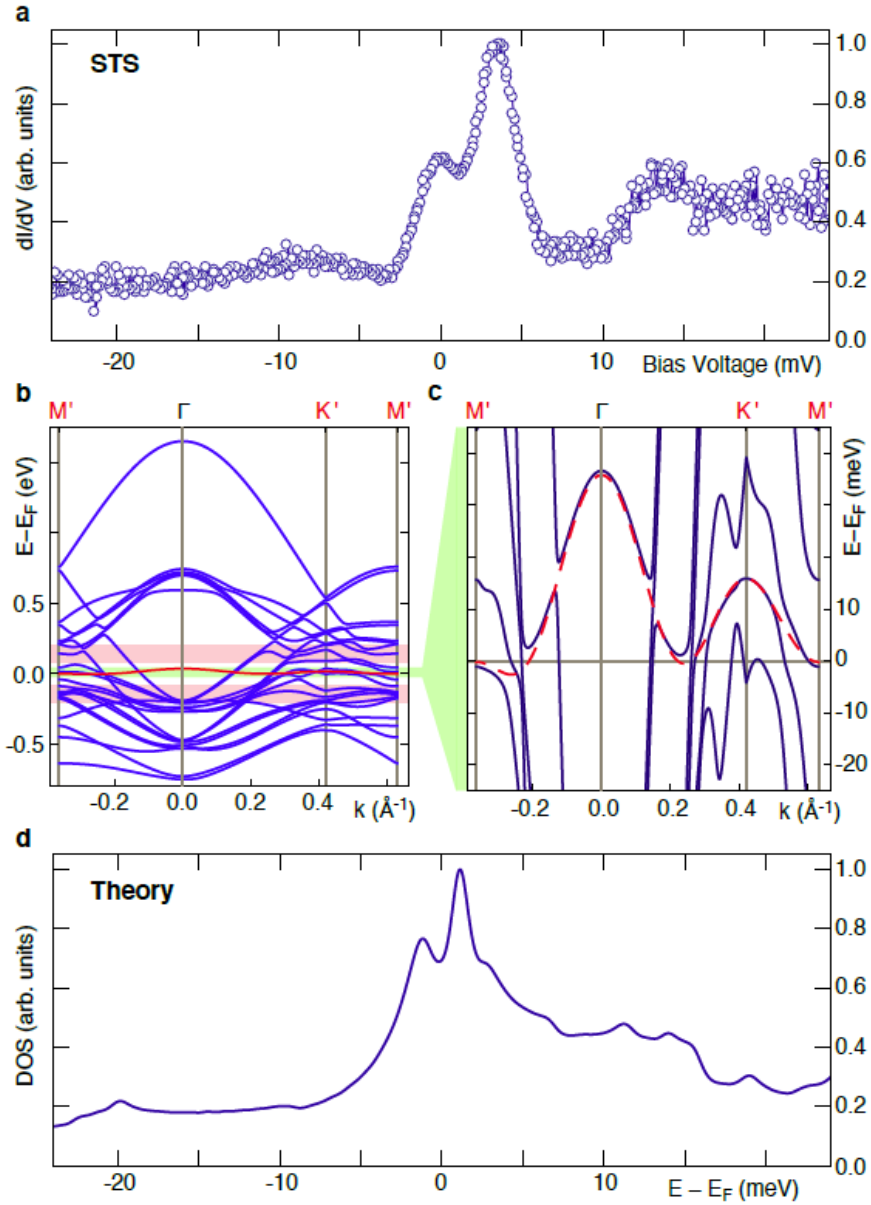


**Figure 4: Kondo lattice DOS at the Fermi level.** **a** High-resolution STS spectrum measured with 200  $\mu\text{V}$  bias modulation at 1.5 K on the 1T/2H single layer region of the TaS<sub>2</sub> crystal. Two peaks separated by 4 meV are clearly resolved close to the Fermi level. **b** Blue lines show the band structure (along the high symmetry

M'ΓK'M' BZ-path) obtained from the bands of the optimized ( $3 \times 3$ ) CDW reconstruction of the 2H-TaS<sub>2</sub> substrate for  $k_z=0$ . The impurity band is at the Fermi level (red line). The position of the Upper and Lower Hubbard sub-bands are marked with two red strips. **c** Zoom in of the band structure shown in panel b close to the Fermi level after an interaction potential  $V_k = 5\text{meV}$  between the impurity band and all conduction states is switched-on (the unperturbed impurity band is depicted as a red-dashed line for reference). **d** Calculated DOS for the system whose band structure is shown in c: a two-peak structure at the Fermi level is predicted in agreement with the experiment.

## Discussion

From the energetics of the single Kondo impurity regime ( $T_K$ ) and the Kondo lattice regime ( $T_{KL}$ ), the Kondo lattice gap should disappear at a temperature  $T_{KL} < T_K$ . Figure 5 shows six selected spectra (black dots are experimental data) from a temperature series recorded using 500  $\mu\text{V}$  bias modulation (see section 8 in the SI for the full series). All spectra have been measured at the center of the SoD in the 1T-TaS<sub>2</sub> layer lying on top of the 2H-TaS<sub>2</sub> crystal. The 500  $\mu\text{V}$  bias modulation is a compromise value between being able to resolve the Kondo lattice gap and keeping a low acquisition time in order to minimize the effects of thermal drift. In addition, for a better visualization the  $dI/dV$  signal background has been subtracted as described in the SI. The top left spectrum of Fig. 5 was measured at 1.7 K, comparing this spectrum with that shown in Fig. 4 for a modulation of 200  $\mu\text{V}$ , both present the same gap-like structure, i.e., a double peak separated by about 4 meV, and a small peak at about +12 meV (see SI section 8 for more details). The other two spectra in the top row of Fig. 5 are measured at 4.2 K and 6.6 K. In both spectra, the gap-like structure associated with the formation of the Kondo lattice can still be seen as a clear asymmetry in the Kondo resonance. The overall intensity of the signal decreases with temperature as expected. The three spectra of the lower row, measured at higher temperatures, are represented with a factor 2 magnification in the vertical scale. In the 7.5 K spectrum, a slight asymmetry in the peak can still be seen, while in the 9.6 K and 12.1 K ones this feature is hardly visible.

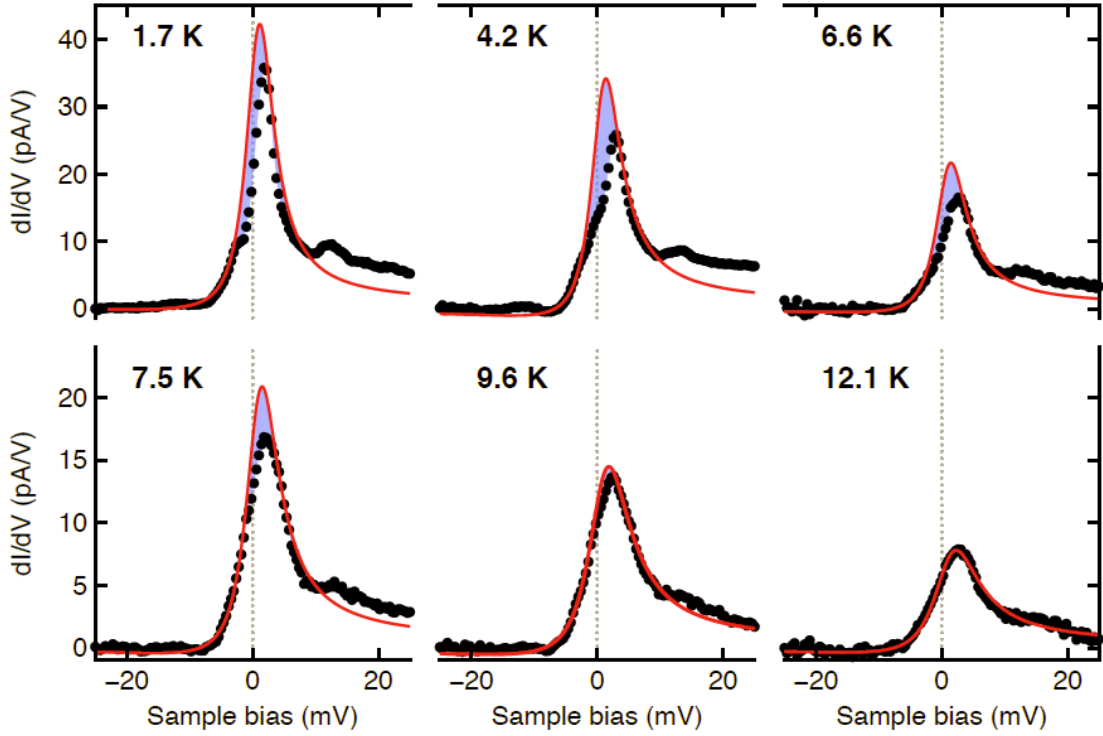


**Figure 5: Temperature dependence of the Kondo lattice gap.** STS spectra from a high energy resolution temperature series. The red lines are Fano fits to the experimental data (black dots) excluding the  $\pm 3$  mV energy range, as explained in section 7 of the SI. The blue shaded area highlights the difference between the “ideal” Fano line-shape and the actual data and represents the LDOS depletion associated to the Kondo lattice gap. Due to the intensity reduction of the Kondo signal at higher temperatures, the vertical scale for the spectra in the lower row is upscaled by a factor 2. STS parameters:  $V=25$  mV,  $I=500$  pA,  $V_{\text{mod}}=500$   $\mu$ V.

To analyze the suppression of the Kondo lattice features in our STS data as a function of temperature, we have computed the area difference between the “ideal” or “gapless” Fano line-shapes (red curves in Fig. 5) and the actual STS data (black dots), see SI section 9 for the details. This area, which can be interpreted as the LDOS depletion associated to the Kondo lattice gap [22, 23], is highlighted in blue in Fig. 5 and represented as a function of temperature in the main graph of Fig. 6 (yellow squares), where the vertical scale is normalized to define as 1 the projected area at zero temperature. The area is gradually reduced as the temperature increases and vanishes above 11 K. This observation cannot be attributed to thermal broadening alone. This is demonstrated by calculating the thermal attenuation of an ideal and temperature-independent 3 meV wide gap on a Kondo resonance modelled with the parameters obtained experimentally in this work (see SI section 10). In the upper insets of Fig. 6 we present the resulting area difference between these ideal gapless (light color) and gapped (dark color) Kondo resonances for four selected temperatures. The complete temperature evolution of the resulting gap area is represented as the brown dashed curve in the main graph, demonstrating that the experimentally observed area drop

cannot be attributed to a thermal attenuation effect. Therefore, we conclude that the experimentally observed area drop presented in Fig. 6 corresponds to the annihilation of the Kondo lattice gap due to the loss of coherence of the heavy-fermion liquid phase. A linear fit to the experimental data (orange curve in figure 6) yields a transition temperature of  $T_{KL} = 11.1\text{K}$ .

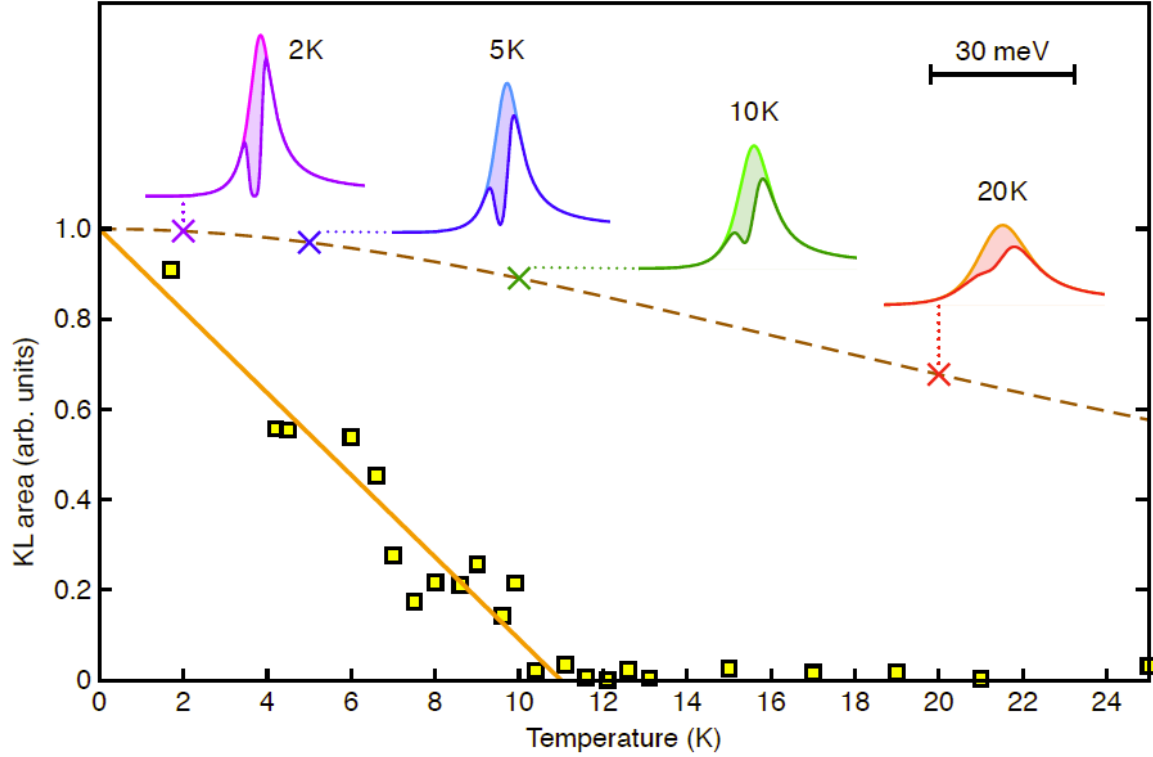


**Figure 6: Temperature evolution of the Kondo lattice gap and expected thermal broadening effect.** The main graph shows the temperature evolution of the area associated to the Kondo lattice gap, given by the blue shaded area in Fig. 5, represented as the yellow filled squares. The area becomes practically negligible above 10 K. A linear fit (orange line) yields a transition temperature  $T_{KL} = 11.1\text{K}$ . The brown dashed line represents the thermal attenuation effect on an ideal and temperature-independent 3 meV wide gap on a Kondo resonance with similar parameters as the one observed experimentally, showing a much slower decay as compared to the observed Kondo lattice gap. In both cases, the vertical scale is normalized so that the area at zero temperature is defined as 1. Upper insets show the gapless (light color curves) vs gapped (dark color curves) Kondo resonances calculated for the ideal gap case and corresponding area differences for four selected temperatures. These correspond to the four points of the thermal attenuation curve highlighted with the crosses colored accordingly.

In summary, we have demonstrated the existence of a Kondo lattice at temperatures below 11 K in a system formed by a 1T-TaS<sub>2</sub> layer deposited on top of a metallic 2H-TaS<sub>2</sub> crystal. The emergence of this new coherent phase over the whole lattice manifests as a double peak structure at the Fermi level, in contrast with the single Kondo regime reached at temperatures between 11K and the Kondo temperature (28K), where a single peak is observed. The presence of a charge density wave imposes a geometrically frustrated 2D lattice to the Mott localized electrons, thus

leading to the formation of a magnetically frustrated Kondo lattice without f electrons. Our work demonstrates that the creation of atomically thin strongly correlated materials with tailored dimensionality, periodicity and symmetry is a real possibility. Thus, these results pave the way for the use of this class of materials in technological applications.

## Methods

**Tip sample preparation.** The 2H-TaS<sub>2</sub> single crystal was exfoliated at room temperature in Ultra-High Vacuum (UHV) using a Nito tape and then it was transferred to the Low Temperature STM without breaking the UHV conditions. The experiments were performed in two different temperature regimes, first, with the STM cooled with liquid nitrogen pumped down to lower the base temperature to 52K and, second, with the STM cooled by a 4He Joule-Thompson stage attaining a base temperature of 1.2 K. The STM tips were home-made by electrochemical etching of a tungsten wire and cleaned in UHV by argon sputtering. Before the experiments the tips were checked against a Cu(111) sample to ensure that they presented a flat density of states at the Fermi level resolving the well-known Cu(111) surface state without any additional features, especially around the Fermi level.

**STS measurements.** The STS spectra have been measured using a lock-in amplifier, adding a certain modulation to the sample bias voltage signal. Two modulation amplitude ranges were employed, a high amplitude (low energy resolution) range above 4mV, and a low amplitude (high energy resolution) range below 500  $\mu$ V, depending on the particular experiment. In all cases the modulation frequency was 763 Hz. All spectra were acquired with the feedback off using a stabilization bias usually between +400 mV to +500mV, away from the Hubbard sub-bands to minimize the influence of the surface electronic structure on the height of the STM tip over the sample.

**Theoretical calculations.** DFT calculations for the 2H phase of the bulk TaS<sub>2</sub> solid have been carried out within the PAW method [42] as implemented in the VASP package [43-45]. We used a 350 eV plane wave cut off and the PBE exchange correlation functional [46]. We adopted a very strict  $10^{-6}$  eV convergence criterion for the self consistent electronic cycles, whereas all the geometry optimizations have been carried out optimizing the position of all the atoms until the maximum residual force was lower than  $10^{-3}$  eV/Å. In the DFT geometry optimizations we adopted  $(18 \times 18 \times 4)$  Monkhorst-Pack (MP) grids [47] to sample the Brillouin Zone (BZ) of the  $(1 \times 1)$  in plane unit cell calculations and  $(6 \times 6 \times 4)$  grids for the  $(3 \times 3)$  in plane unit cell calculations. Each single layer 2H-TaS<sub>2</sub> is characterized by a Ta hexagonal lattice sandwiched between two S hexagonal lattices with the Ta atoms sitting at the center of a trigonal prism, whose corners are occupied by the S atoms. The bulk 2H-TaS<sub>2</sub> material is obtained stacking the single layers so that the Ta atoms of neighboring layers are stack one on top of the other, whereas the S lattices of neighboring layers are rotated by 60° one with respect to the other (like in the AB stacking of graphite). Our DFT calculations have demonstrated that this AB stacking is indeed energetically

avored with respect to the AA' stacking usually common to TMDs containing Mo and W [48]. Due to the dispersive nature of the inter-plane interaction of the TaS<sub>2</sub> layers in the bulk, we included in the calculation the Grimme D3 correction [49] to the PBE functional, which has proven to be effective in reproducing both the in-plane and the out of plane lattice constants of relevant TMDs [50].

## References

1. D. Aoki, A. Huzley, E. Ressouche, D. Braithwaite, J. Flouquet, J. P. Brison, E. Lhotel, C. Paulsen, Coexistence of superconductivity and ferromagnetism in URhGe. *Nature* **413**, 613-61 (2001).
2. N.T. Huy, A. Gasparini, D. E. de Nijs, Y. Huang, J. C. P. Klaasse, T. Gortenmulden, A. de Visser, A. Hamann, T. Görlach, H. V. Löhneysen, Superconductivity on the border of weak itinerant ferromagnetism in UCoGe. *Phys. Rev. Lett.* **99**, 067006 (2007).
3. G. Riblet, K. Winzer, Vanishing of superconductivity below a second transition temperature in (La<sub>1-x</sub>Ce<sub>x</sub>)Al<sub>2</sub> alloys due to the Kondo effect. *Solid State Commun.* **9**, 1663-1665 (1971).
4. F. Lévy, I. Sheikin, B. Grenier, A.D. Huxley, Magnetic field-induced superconductivity in the ferromagnet URhGe. *Science* **309**, 1343-1346 (2005)
5. H.Q. Yuan, F. M. Grosche, M. Deppe, G. Geibel, G. Sparn, F. Steglich, Observation of two distinct superconductive phases in CeCu<sub>2</sub>Si<sub>2</sub>. *Science* **302**, 2104-2107 (2003).
6. M. Nakano, K. Shibuya, D. Okuyama, T. Hatano, S. Ono, M. Kawasaki, Y. Iwasa, Y. Tokura, Collective bulk carrier delocalization driven by electrostatic surface charge accumulation. *Nature* **487**, 459-462 (2012).
7. P. Schneider, M. Schmitt, J. Gabel, M. Zapf, M. Stübinger, P. Schütz, L. Dudy, C. Schlueter, T-L. Lee, M. Sing, R. Claessen, Tailoring materials for Mottronics: Excess oxygen doping of a prototypical Mott insulator. *Adv. Mater.* **30**, 1706708 (2018).
8. G. R. Stewart, Heavy-Fermion systems. *Rev. Mod. Phys.* **56**, 755-787 (1984).
9. M. A. Ruderman, C. Kittel, Indirect exchange coupling of nuclear magnetic moments by conduction electrons. *Phys. Rev.* **96**, 99-102 (1954).
10. T. Kasuya, A theory of metallic Ferro- and Antiferromagnetism on Zener's model. *Prog. Theor. Phys.* **16**, 45-57 (1956).
11. K. Yosida, Magnetic properties of Cu-Mn alloys. *Phys. Rev.* **106**, 893-898 (1957).
12. P.W. Anderson, Localized magnetic states in metals. *Phys. Rev.* **124**, 41-53 (1961).
13. J. Kondo, Resistance minimum in diluted magnetic alloys. *Prog. Theor. Phys.* **32**, 37-49 (1964).
14. J. R. Schrieffer, P. A. Wolf, Relation between the Anderson and Kondo hamiltonians. *Phys. Rev.* **149**, 491-492 (1966).
15. S. Doniach, The Kondo lattice and weak antiferromagnetism. *Physica B & C* **91**, 231-234 (1977).
16. W. R. Johanson, G. W. Crabtree, A. S. Edelstein, O. D. McMasters, Fermi-surface measurements of mixed-valence CeSn<sub>3</sub>. *Phys. Rev. Lett.* **46**, 504-507 (1981)

17. Y.-F. Yang, Z. Fisk, H.-O. Lee, J. D. Thompson, D. Pines, Scaling the Kondo lattice. *Nature* **454**, 611-613 (2008).
18. A. R. Schmidt, M. H. Hamidian, P. Wahl, F. Meier, A. V. Balatsky, J. D. Garret, T. J. Williams, G. M. Luke, J. C. Davis. Imaging the Fano lattice to “Hidden order” transition in URu<sub>2</sub>Si<sub>2</sub>. *Nature* **465**, 570-576 (2010).
19. S. Ernst, S. Kirchner, C. Geibel, G. Zwicknagl, F. Steglich, S. Wirth, Emerging local Kondo screening and spatial coherence in the heavy-fermion metal YbRh<sub>2</sub>Si<sub>2</sub>. *Nature* **474**, 362-366 (2011).
20. P. Aynajian, E. H. da Silva Neto, A. Gyenis, R. E. Baumbach, J. D. Thompson, Z. Fisk, E. D. Bauer, A. Yazdani, Visualizing heavy-fermions emerging in a quantum critical Kondo lattice. *Nature* **486**, 201-206 (2012).
21. P. Coleman, A.H. Nevidomskyy, Frustration and the Kondo effect in heavy fermion materials. *J. Low Temp. Phys.* **161**, 182-202 (2010).
22. R.M. Martin, Fermi-surface sum rule and its consequences for periodic Kondo and mixed-valence systems. *Phys. Rev. Lett.* **48**, 362-365 (1982).
23. A. C. Hewson, “The Kondo problem to Heavy fermions”, Cambridge University Press, Cambridge (1993).
24. P. Fulde, J. Keller, G. Zwicknagl, Theory of heavy fermion systems. *Solid State Phys.* **41**, 1-150 (1988).
25. V. Madhavan, W. Chen, T. Jamneala, M. F. Crommie, N. S. Wingreen, Tunneling into single magnetic atom: Spectroscopic evidence of the Kondo resonance. *Science* **280**, 567-569 (1998).
26. M. Ternes, A. J. Heinrich, W.-D. Schneider, Spectroscopic manifestation of the Kondo effect on single adatoms. *J. Phys.: Condens. Mater* **21**, 053001 (2009).
27. M. Garnica D. Stradi, S. Barja, F. Calleja, C. Díaz, M. Alcamí, N. Martín, A. L. Vázquez de Parga, F. Martín, R. Miranda, Long-range magnetic order in a purely organic 2D layer adsorbed on epitaxial graphene. *Nat. Phys.* **9**, 368-374 (2013).
28. J. A. Wilson, A. D. Yoffe, The transition metal dichalcogenides discussion and interpretation of the observed optical, electrical and structural properties. *Adv. Phys.* **18**, 193-335 (1969).
29. J. A. Wilson, F. J. Di Salvo, S. Mahajan, Charge-density waves and superlattices in the metallic layered transition metal dichalcogenides. *Adv. Phys.* **24**, 117-201 (1975).
30. Z. Wang, Y. Y. Sun, I. Abdelwahab, L. Cao, W. Yu, H. Ju, J. Zhu, W. Fu, L. Chu, H. Xu, K. P. Loh, Surface-limited superconducting phase transition on 1T-TaS<sub>2</sub>. *ACS Nano* **12**, 12619-12628 (2018).
31. G. A. Scholz, O. Singh, R. F. Frindt, A. E. Curzon, Charge density wave commensurability in 2H-TaS<sub>2</sub> and Ag<sub>x</sub>TaS<sub>2</sub>. *Solid State Commun.* **44**, 1455-1459 (1982).
32. C. Wang, B. Giambattista, C. G. Slough, R. V. Coleman, M. A. Subramanian, Energy gaps measured by scanning tunneling microscopy. *Phys. Rev. B* **42**, 8890-8906 (1990).

33. W. C. Tonjes, V. A. Greanya, R. Liu, C. G. Olson, P. Molinié, Charge-density-wave mechanism in the 2H-NbSe<sub>2</sub> family: Angle-resolved photoemission studies. *Phys. Rev. B* **63**, 235101 (2001).
34. B. Giambattista, C. G. Slough, W. W. McNairy, R. V. Coleman, Scanning tunneling microscopy of atoms and charge-density waves in 1T-TaS<sub>2</sub>, 1T-TaSe<sub>2</sub>, and 1T-VSe<sub>2</sub>. *Phys. Rev. B* **41**, 10082 (1990).
35. N. V. Smith, S. D. Kevan, F. J. DiSalvo, Band structure of layered compounds 1T-TaS<sub>2</sub> and 2H-TaSe<sub>2</sub> in the presence of commensurate charge-density wave. *J. Phys. C* **18**, 3175-3189 (1985).
36. K. Rossnagel, N. V. Smith, Spin orbit coupling in the band structure of reconstructed 1T-TaS<sub>2</sub>. *Phys. Rev. B* **73**, 073106 (2006).
37. R. Manzke, T. Buslaps, B. Pfalzgraf, M. Skibowski, O. Anderson, On the phase transition in 1T-TaS<sub>2</sub>. *Europhys. Lett.* **8**, 195-200 (1989).
38. P. Fazekas, E. Tosatti, Electrical, structural and magnetic properties of pure and doped 1T-TaS<sub>2</sub>. *Philos. Mag. B* **39**, 229-244 (1979).
39. W. Ruan, Y. Chen, S. Tang, J. Hwang, H-Z. Tsai, R. L. Lee, M. Wu, H. Ryu, S. Kahn, F. Liou, C. Jia, A. Aikawa, C. Hwang, F. Wang, Y. Choi, S. G. Louie, P. A. Lee, Z-X. Shen, S-K Mo, M. F. Crommie, Evidence from quantum spin liquid behaviour in single layer 1T-TaSe<sub>2</sub> from scanning tunnelling microscopy. *Nat. Phys.* **17**, 1154-1161 (2021).
40. V. Vaño, M. Amini, S. C. Ganguli, G. Chen, J. L. Lado, S. Kezilebieke, P. Lilijeroth, Artificial heavy fermions in a van der Waals heterostructure. *Nature* **599**, 582-586 (2021).
41. K. T. Law, P. A. Lee, 1T-TaS<sub>2</sub> as a quantum spin liquid. *Proc. Natl. Acad. Sci.* **114**, 6996-7000 (2017).
42. P. E. Blöchl, Projector augmented-wave method. *Phys. Rev. B.* **50**, 17953–17979 (1994).
43. G. Kresse, D. Joubert, From ultrasoft pseudopotentials to the projector augmented-wave method. *Phys. Rev. B.* **59**, 1758–1775 (1999).
44. G. Kresse, J. Furthmüller, Efficiency of ab-initio total energy calculations for metals and semiconductors using a plane-wave basis set. *Computational Materials Science.* **6**, 15–50 (1996).
45. G. Kresse, J. Furthmüller, Efficient iterative schemes for *ab initio* total-energy calculations using a plane-wave basis set. *Phys. Rev. B.* **54**, 11169–11186 (1996).
46. J. P. Perdew, K. Burke, M. Ernzerhof, Generalized gradient approximation made simple. *Phys. Rev. Lett.* **77**, 3865–3868 (1996).
47. H. J. Monkhorst, J. D. Pack, Special points for Brillouin-zone integrations. *Phys. Rev. B.* **13**, 5188–5192 (1976).
48. J. He, K. Hummer, C. Franchini, Stacking effects on the electronic and optical properties of bilayer transition metal dichalcogenides MoS<sub>2</sub>, MoSe<sub>2</sub>, WS<sub>2</sub>, and WSe<sub>2</sub>. *Phys. Rev. B.* **89**, 075409 (2014).

49. S. Grimme, S. Ehrlich, L. Goerigk, Effect of the damping function in dispersion corrected density functional theory. *J. Comput. Chem.* **32**, 1456–1465 (2011).
50. M. Pisarra, C. Díaz, F. Martín, Theoretical study of structural and electronic properties of 2H-phase transition metal dichalcogenides. *Phys. Rev. B.* **103**, 195416 (2021).